A review on atom probe and correlative microscopy studies of corrosion in nickel-based superalloys

C. Rodenkirchen,* M. Appleton, M.P. Ryan, and S. Pedrazzini

This article discusses challenges faced in the development of new Ni-based superalloys for applications in the hottest sections of turbine engines and the use of atom probe tomography and correlative microscopy for characterization of these complex alloys with regards to microstructural and compositional design. The two strengthening phases γ and γ′ are introduced and the precipitation of topologically close-packed phases and their potential detrimental effects on superalloy properties are reviewed. Mechanisms of environmental degradation, namely oxidation and hot corrosion, are elucidated and recent research studies on a new phenomenon of hot corrosion at relatively low temperatures below 600°C are discussed. The effect of individual alloying elements on superalloy properties is reviewed, with a focus on Mo and W. The use of atom probe in correlation with state-of-the-art microscopy, spectroscopy and diffraction techniques to study and understand oxidation and corrosion of Ni-based superalloys, including crack tip investigations, is presented.

Introduction

Materials with extraordinary properties are needed to operate in the hottest parts of gas-turbine engines of commercial aircrafts, such as the 1st stage turbine blades (**Figure 1**).[1] In addition to mechanical strength, they must also resist corrosion from environmental contaminants from route-dependent ingestions such as desert sand or halide-containing seawater.[2]

Ni-based superalloys exhibit outstanding mechanical strength and creep resistance at temperatures close to their melting points. Their compositions (involving 10–14 alloying elements) and preparation methods are tailored to the operating conditions of turbine blades, and their development is ongoing. For example, a developmental alloy TMS238 of the latest generation (not currently employed in-service) excels with a creep rupture life of 2000 h at 1100°C, 137 MPa, several hundred hours longer than the current commonly applied second-generation superalloy CMSX-4.[4] The operating temperatures are, however, so extreme that high-performance superalloys are further protected by internal cooling passages, antioxidation coatings, and thermal barrier coatings.[2,5]

Over the past 40 years, superalloy development led to substantial changes both in their fabrication and in their composition. From expensively wrought to cast fabrication and the successive reduction of grain-boundary (GB) formation in turbine blade alloys, today, turbine blades are cast as single crystals for best high-temperature properties, whereas the larger turbine discs are polycrystalline powder processed.[5] Superalloy compositions evolved as the benefits of new alloying additions were discovered, which has resulted in six generations thus far.[2,5–7]

Key goals in the development of new superalloys are strength and phase stability at increasingly elevated temperatures, as increased turbine entry temperatures translate into improved efficiency and reduced fuel consumption—reducing carbon emissions and costs.[8] However, resistance against environmental degradation is also crucial and often neglected. Traditionally, superalloy development has focused on increasing creep resistance with comparatively less research being performed on corrosion resistance. The recent discovery of new, unexpected corrosion mechanisms at temperatures as low as 500°C has led to renewed interest in corrosion research.[2,4,9] The interplay of alloying effects on the various required superalloy characteristics is complex and further research is needed to elucidate the underlying thermodynamic and kinetic mechanisms, and to use this knowledge to further improve nickel-based superalloys.

C. Rodenkirchen, Department of Materials, Imperial College London, Royal School of Mines, London, UK; c.rodenkirchen20@imperial.ac.uk
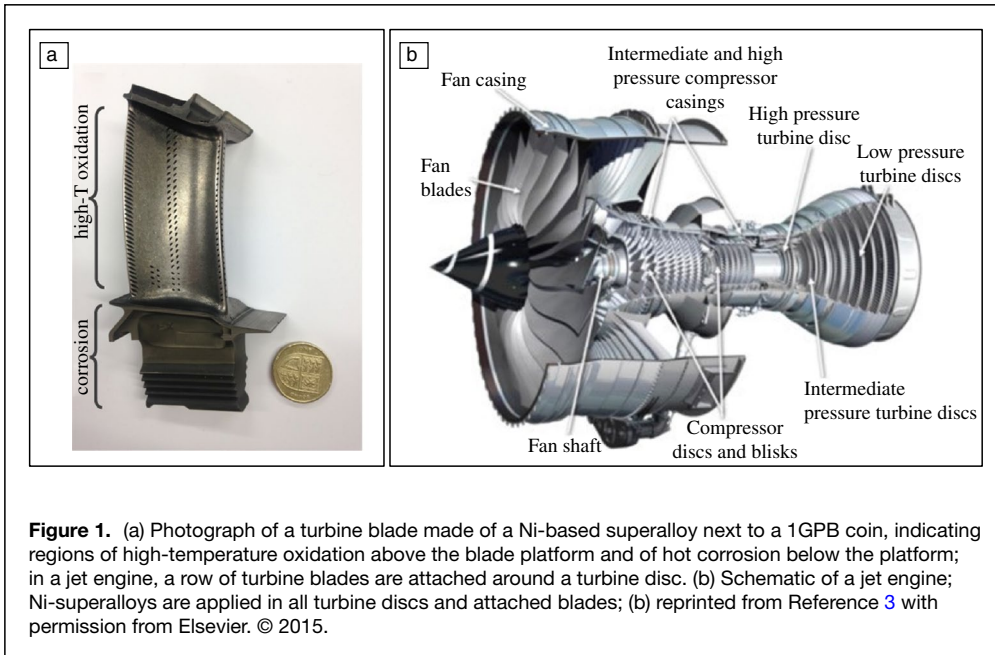M. Appleton, Rolls-Royce plc, Derby, UK; matt.appleton@rolls-royce.com
M.P. Ryan, Department of Materials, Imperial College London, Royal School of Mines, London, UK; m.p.ryan@imperial.ac.uk
S. Pedrazzini, Department of Materials, Imperial College London, Royal School of Mines, London, UK; s.pedrazzini@imperial.ac.uk
*Corresponding author

Figure 1. (a) Photograph of a turbine blade made of a Ni-based superalloy next to a 1GPB coin, indicating regions of high-temperature oxidation above the blade platform and of hot corrosion below the platform; in a jet engine, a row of turbine blades are attached around a turbine disc. (b) Schematic of a jet engine; Ni-superalloys are applied in all turbine discs and attached blades; (b) reprinted from Reference 3 with permission from Elsevier. © 2015.

underpinning corrosion and stress-corrosion cracking.[11–13]

This article discusses current scientific knowledge of nickel-superalloys and the role of alloying additions on phase stability and corrosion resistance, with a particular emphasis on additions of W and Mo—known for improving creep resistance. The use of correlative microscopy with atom probe tomography (APT) to understand key oxidation and corrosion mechanisms, including crack investigation is reviewed. APT is deemed a powerful
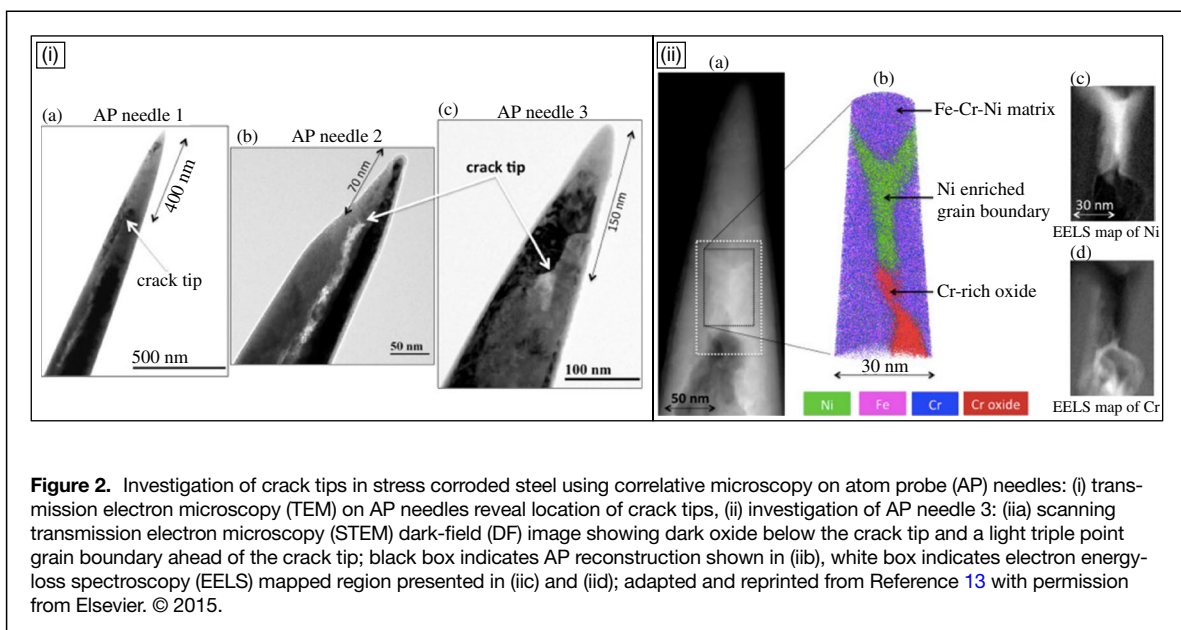
Analyzing the material across a range of length scales up to atomic-scale resolution is critical to develop mechanistic understanding. Recent advances in instrumentation and analytical techniques have allowed substantial improvements in spatial and chemical resolution.[10] Advances in atom probe tomography (APT) as a 3D near-atomic-scale characterization technique have allowed the analysis of delicate oxidized and corroded compounds, including crack tips of interrupted mechanical tests (e.g., **Figure 2**). Through combination of APT with other investigation tools, a broad range of material properties can be characterized at varying length scales and with complementary precision, enabling further understanding of the mechanisms

complement to other, lower resolution investigation techniques such as scanning electron microscopy (SEM), energy-dispersive x-ray spectroscopy (EDX), and x-ray diffraction (XRD) that enabled unprecedented insights in the mechanisms underpinning corrosion, oxidation, phase stability, and strength.

Nickel-based superalloys: Microstructure and strengthening mechanisms

The γ and γ' phases

Ni-based superalloys owe their outstanding mechanical properties to the interplay of two phases: cuboidal γ' phase precipitates in a γ phase matrix.[5,14] The γ matrix phase consists

Figure 2. Investigation of crack tips in stress corroded steel using correlative microscopy on atom probe (AP) needles: (i) transmission electron microscopy (TEM) on AP needles reveal location of crack tips, (ii) investigation of AP needle 3: (iia) scanning transmission electron microscopy (STEM) dark-field (DF) image showing dark oxide below the crack tip and a light triple point grain boundary ahead of the crack tip; black box indicates AP reconstruction shown in (iib), white box indicates electron energy-loss spectroscopy (EELS) mapped region presented in (iic) and (iid); adapted and reprinted from Reference 13 with permission from Elsevier. © 2015.

of face-centered-cubic (fcc) Ni.[1,5,14,15] The γ' phase exhibits an ordered L1$_2$ crystal structure with nickel atoms situated at the face centers and aluminum atoms situated at the unit cell corners.[5] Titanium and tantalum can substitute for Al atoms because of their relatively large diameter, similar to that of Al, whereas smaller atoms can substitute for Ni, which is usually the smallest element in a superalloy.[1,5]

Dendritic segregation during superalloy casting leads to enrichment of Cr, Co, Re, W, and Mo in dendrite cores and of Al, Ti, and Ta in interdendritic regions.[16] To homogenize the elemental distribution a solution-heat treatment is applied, followed by an aging heat treatment to attain the desirable formation of similarly sized, regularly stacked, cuboidal γ' precipitates with dimensions of around 300–500 nm (**Figure 3**).[2,5,14] Their cuboid faces lie in the (100)-planes and are coherent with the γ phase.[5,17] Optimal superalloy properties are achieved for this shape and γ' volume fractions of 40–75%[1,5] such that a tight tile-like pattern arises with thin γ channels filling the gaps between the γ' precipitates. The γ' phase confers high-temperature strength to Ni-based superalloys, due to its anomalous yield effect: unlike most other known materials, its yield strength increases with temperature (up to a maximum) due to a dislocation cross-slip mechanism, which renders them temporarily sessile. However, γ' is extremely brittle, therefore optimal properties are achieved only in combination with the γ phase, resulting in a stable yield strength up to 800°C[1] and strongly improved creep rupture life and tensile strength.[14]

The γ phase is strengthened through solid-solution strengthening by larger elements than Ni (e.g., Cr, Re, Mo, W, Co).[2,14] The resulting lattice distortion increases the shear moduli and

diminishes dislocation movement in the γ phase.[5] The heavier elements Mo, W, and Re positively affect creep resistance as they exhibit relatively low diffusion rates in Ni, notably lower than Ni.[14,19,20]

Phase stability and TCP phase formation

Although the γ and γ' phase formation is desirable, other detrimental phases can form if the alloy is not thermodynamically phase-stable. The term topologically close-packed (TCP) phases comprises several types of undesirable phases, which can form during long-term heat treatment, including extended times in service.[21,22]

Refractory elements such as Mo, W, and Re are mainly added to superalloys to increase creep strength.[19] However, excessive additions lead to a higher probability for TCP formation, especially in turbine blades where the γ' volume fraction is large and hence the TCP phase forming elements (Cr, Co, Mo, W, Re), most of which preferentially partition to the γ phase, are more strongly concentrated locally.[19,21] Microsegregation of refractories to the dendrite cores has also been associated to TCP formation,[23] especially with regard to Re, having slow diffusion rates in Ni, several orders of magnitude lower than other alloying elements.[20,23,24]

TCP phases are detrimental to superalloy properties[1,25] although at low volume fractions no deterioration is observed.[23,26] The exact role of these phases in the failure of Ni-superalloys is still debated.[22] TCP phases deplete the γ phase of its solid-solution strengtheners Re, W, Mo, and Cr,[21] which may reduce the alloy's creep strength.[27] Additionally, due to their brittleness, TCP phases are prone to cracking.[5]

Although some studies suggest that TCP cracking is not detrimental as it is purely internal and does not propagate outside the precipitate,[21,26] other studies have associated microcrack initiation near TCP phases with crack propagation through the alloy.[28]

As turbine blades are exposed to stress during service, the effect of stress on TCP phases is an alloy design consideration. Stress is known to affect TCP phases,[26] although its extent varies strongly with the overall superalloy composition.[21] In some alloys with (W + Mo) content higher than 16 wt%, precipitation of
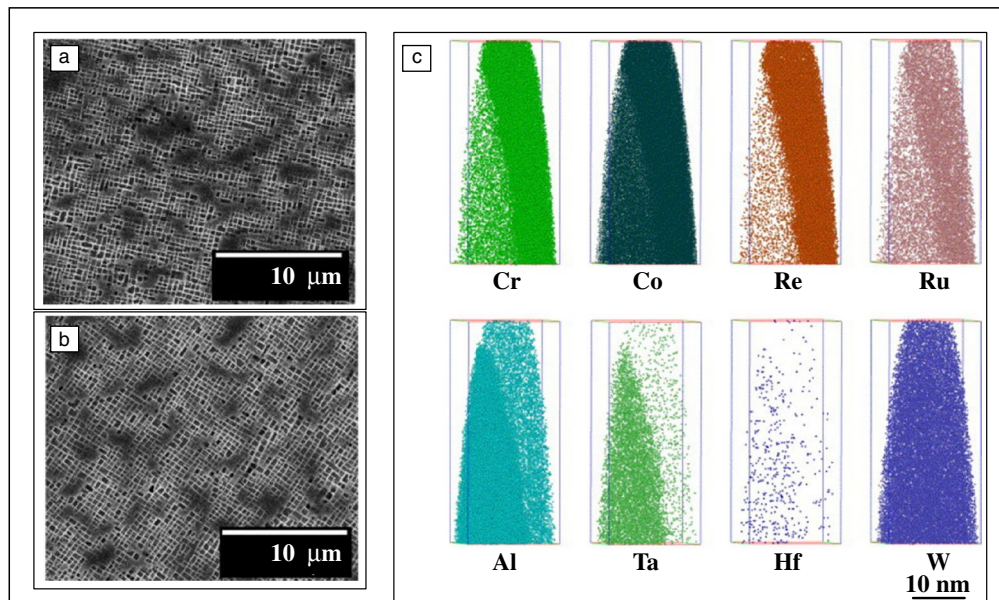

Figure 3. (a, b) Typical microstructure of Ni-based superalloys exhibiting cuboidal γ' precipitates between γ channels; (c) atom probe needle taken from samples depicted in (a, b) revealing elemental partitioning between the phases; Al, Ta partitions to γ' (bottom left), whereas Cr, Co, Re, Ru partition to γ'; adapted and reprinted from Reference 18 with permission from Elsevier. © 2004.

TCP α-(W,Mo) was observed.[29,30] However, this composition far exceeds the (W+Mo) content in most commercially used alloys.

The W:Mo ratio also affects the type and severity of TCP phase precipitation in a superalloy. At identical (W+Mo) wt. composition, an alloy with higher W:Mo ratio (6.5:1.5) led to extensive needle-shape μ phase precipitation after only 1500 h heat treatment at 950°C, while a lower W:Mo ratio alloy (5.5:2.5) precipitated only submicron scale P phase precipitates after up to 10,000 h at 905°C. The authors related this to a suppressed dendrite core segregation of the elements Re and W, and to reduced Cr and Re partitioning to the γ channels after extended heat treatment.[25]

Environmental degradation

Oxidation

As a superalloy is exposed to reactive elements in the environment, oxidation reactions occur that can either be beneficial or detrimental to its properties. A common protection strategy is selective oxidation of one of the alloy components, which then forms a protective barrier between the environment and the alloy.[31] A protective oxide forms a continuous, slow-growing, passivating scale with good adhesion to the underlying alloy. Its thickness should be about 1–20 μm. Slower growth rates are unlikely to result in a continuous and protective layer, whereas faster growing scales are prone to spallation.[2,32] The most protective oxides tend to be chromia (Cr_2O_3) or alumina (Al_2O_3).[31,33] Although Cr_2O_3 is only protective up to 1000–1100°C (it forms volatile CrO_3 at higher temperatures), Al_2O_3 is protective up to 1300–1400°C.[31,32] Hence, superalloys for high-temperature applications such as turbine blades are alumina formers.[14,34]

Thermodynamically, oxidation is governed by the Gibbs free energy G of the system, where the most stable state is reached for minimized G. Considering all possible oxides, the ones leading to the strongest reduction in G are stable and will form the oxide scale. Among those, oxides that need a higher oxygen partial pressure p_O are found at the oxide-gas interface, whereas others can form further below the surface.[35] If the oxidation process is diffusion-controlled (i.e., if the oxide scale is continuous and adheres well to the metal surface), it slows down after the first thin layer of oxide has formed and the reactants must diffuse through the oxide scale before the reaction can continue.[31]

Selective oxidation is generally considered the basis for long-term protection of the alloy by means of surface passivation.[31] The respective alloying element must diffuse quickly to the alloy/scale interface to oxidize as a continuous layer. If the elemental concentration is too low, or diffusion too slow, internal oxidation can occur, which can be detrimental to fatigue properties. Since diffusion can be affected by surface finish (e.g., machining an alloy leads to subsurface defects, which facilitate and accelerate external scale growth), it is crucial to perform oxidation studies on samples with a controlled surface finish.[33]

Typically, during the initial, transient stage of oxide scale growth, all alloying elements near the surface form oxides.[33] When the subsurface region is depleted in elements that form rapid-growing oxides, the slower-growing and thermodynamically more stable oxides (e.g., Cr_2O_3 or Al_2O_3) consume and replace the initial, nonprotective oxides, forming a continuous, protective scale.[2,31] In the steady-state stage, selective oxidation occurs: growth of the other oxides is inhibited by the prevailing low p_O at the alloy-scale interface[31] as well as low diffusivity within the scale, which hinders oxide growth above the protective scale.[32]

Oxide scale spallation can occur during thermal cycling due to stresses associated with differing coefficients of thermal expansion of the scale and the alloy.[32] Regrowth of the oxide scale can be difficult or even impossible as the subsurface alloy region is depleted in its oxidizing element.[31,36] Spallation is also promoted by sulfur and by voids.[33]

In addition, the effect of minor alloying elements such as silicon,[37,38] boron,[39] or titanium[40,41] can profoundly alter oxidation behavior, although the underlying mechanisms are not currently understood. Some considerations are required when explaining the effect of minor alloying elements, namely how they affect the kinetics of oxide scale growth and whether they promote the nucleation of transient or stable oxides. Atom probe, due to its unparalleled spatial and chemical resolution, has been instrumental for the understanding of oxidation kinetics, particularly the effect of trace elements, as discussed in detail in the "Contributions of atom probe tomography and correlative microscopy" section of this article.

Hot corrosion

Contaminant sulfides (such as S, Ca, Na, K) entering the engine from fuel and external sources such as sea salt or volcanic emissions react with oxygen and form various sulfates such as Na_2SO_4.[2,8,42] Fused salt-film deposits on the superalloy surface at elevated temperatures can drive accelerated attacks termed hot corrosion.[8,43] Fluxing is one of the dominant hot corrosion mechanisms, as elaborated by Rapp.[43] It describes the dissolution of the protective oxide layer by a liquid salt-film and its reprecipitation further within the melt as individual oxide particles, having lost their protective character. This mechanism is based on the dependence of the oxide solubility on the acidity of the melt. Continuous hot corrosion occurs if the melt exhibits a negative solubility gradient (i.e., when there is a higher oxide solubility at the superalloy/salt interface than at the salt/gas interface). In this case, the oxide dissolves into the salt layer, but as the solubility decreases further toward the salt/gas interface, nonprotective oxide particles reprecipitate.[43]

Types of hot corrosion

Type I, or high-temperature hot corrosion (HTHC), occurs at temperatures at around 850–950°C when salt condenses

from the gas phase onto the superalloy surface forming the fused salt-film necessary for fluxing.[8] When the salt reaches the superalloy substrate below the oxide scale, it reacts with Ni and Cr to form sulfides, which depletes the subsurface region of Cr.[2,8] HTHC develops in four stages: (1) as the oxide scale starts to break down, the surface roughens; (2) while this continues, the alloy subsurface region becomes depleted in chromium; (3) the superalloy substrate is oxidized to such depths that the mechanical performance can no longer be ensured and the blades should be replaced; (4) finally, the corrosion attack progresses such that material can break off and premature failure can occur. This can be caused by either a loss of cross-sectional area, subjecting the blade to increased internal stresses, or by crack initiation and growth. Microscopically, HTHC is characterized by a porous oxide scale and a subjacent sulfidation and depletion region. On a macroscopic scale, material peeling and color changes are observable.[8]

Type II, or low-temperature hot corrosion (LTHC), occurs at temperatures below the melting temperature of Na_2SO_4, between 600°C and 800°C.[2,8] The mechanisms involved in this type of hot corrosion are not yet fully understood,[44] but typically, salts are deposited on the blade surface as vapor condensates. In an initial incubation stage, they melt as they form eutectics such as Na_2SO_4-Ni_2SO_4 (eutectic temperature T_e = 671°C). The Ni sulfates form through the reaction of the surface oxides with SO_3 from the gaseous environment if a sufficiently high SO_3 partial pressure (p_{SO3}) is provided. In the propagation stage, gas-phase induced fluxing takes place as SO_3 and the liquid deposit progress inward and Ni migrates outward.[2,44–46] LTHC, in contrast to HTHC, commonly results in pitting (i.e., localized cavity formation),[8] which depends heavily on the sulfur contamination. Higher sulfur availability leads to deeper pit formation.[2] Typically, LTHC exhibits increasing sulfur contents toward the base of the pits and a penetration of the superalloy by chromium (or other) sulfides.[47] Besides the characteristic pitting, some cases of continuous attack have been reported (e.g., for alloys that do not develop a protective oxide scale).[42,46] LTHC occurs suddenly, posing a real danger of undetected, catastrophic failures.[8]

Although the temperature range at which hot corrosion occurs is often used to distinguish between type I and type II hot corrosion, the mechanism of liquid formation might be more appropriate for the distinction. Besides the gas-phase induced fluxing typically observed in LTHC, Lutz et al.[47] observed alloy-induced acidic fluxing for Mo-rich disc alloys in the LTHC temperature range (700°C). Sodium molybdate (Na_2MoO_4, not a eutectic) with a melting point of 687°C can form from the reaction of molybdenum oxides in the scale with a Na_2SO_4 deposit in alloys exceeding 2 wt% Mo. The strong acidic melt results in alloy-induced acidic fluxing with no need of gaseous SO_3, exhibiting characteristic HTHC degradation.[47]

Corrosion below 600°C

Recently, the lower parts of the turbine blade, below the blade platform, experiencing lower temperatures around 550°C, have exhibited LTHC.[9,46,48] Little research has been conducted on corrosion below 600°C, although some mechanisms have been proposed. Kistler et al.[44] reported LTHC at 550–650°C (i.e., below the eutectic temperature of Na_2SO_4-Ni_2SO_4, and, although only in an SO_2/SO_3 containing environment, below the eutectic equilibrium p_{SO3}). The corrosion products exhibited (Ni,Co) O at the sulfate/gas interface with localized channels through the Na_2SO_4 deposit. After prolonged heat treatment, this oxide fully consumed the deposit. They reported formation of a previously unreported, nanocrystalline phase enveloping the channels, with composition $Na_2Ni_2SO_5$, although the transmission electron microscopy (TEM)-EDX technique used in this study has known limitations in oxygen measurement. The authors report that corrosion only occurred at temperatures and SO_3 partial pressures at which this phase was stable. They concluded that Ni entered the deposit through the channels that then decomposed into NiO. In contrast to typical LTHC, this mechanism involves a solid-state process instead of liquid formation.[44]

Brooking et al.[9] suggested an LTHC stress-corrosion cracking mechanism for situations of combined SO_3-containing gaseous environment, salt deposit, and tensile load. Specimens of superalloy CMSX-4, commonly employed in turbine engines, were coated with a Na/K sulfate, and subjected to a constant load through three-point bending at 550°C and an air/300 ppm SO_3 environment, to simulate typical in-service conditions of the under-platform turbine blade section. The compressively loaded side exhibited preferential corrosion attack of the γ channels whereas the tensile loaded side showed preferential attack of the γ′ precipitates. Cracks were only observed on the tensile loaded side, cutting through the precipitates. As Na was found within the cracks, Brooking et al. proposed that liquid sodium salts acted as an electrolyte, which in combination with the static load led to an electrochemical stress-corrosion cracking mechanism. This also explains the preferential attack of γ or γ′, respectively, as strain influences the anodic potential of the phases.[9] A previous study reported that cracking did not occur for unstressed specimens nor for specimens without a salt deposit, which confirms crack initiation through the combined or synergistic effects of stress and corrosion.[46]

Chemistry tailoring for optimized material properties

Corrosion must be inhibited to prevent dangerous and costly failures. This can be achieved through the application of protective oxidation-resistant coatings and by developing highly corrosion-resistant superalloys through rational compositional design.[8]

The interplay of the alloying elements is complex and even small compositional changes (<1%) can greatly alter the superalloy properties.[49,50] Fine-tuning of the composition plays a

major role in simultaneously achieving high-temperature mechanical strength and oxidation resistance.[14] Oxidation and corrosion resistance is predominantly given by Al and Cr, forming protective oxide scales.[2,5] Trace amounts of reactive elements (e.g., Y, Hf) can be added,[2] which segregate to oxide grain boundaries and the scale-alloy interface, trapping spallation promoting sulfur.[33] Ru improves long-term stability,[7,51] reducing the probability of TCP phase precipitation by the so-called reverse partitioning effect: increasing the solubility of elements in their usually less favorable phase (i.e., lowering the concentration of TCP formers in the γ channels).[5,49] Ru also reduces dendritic segregation in the as-cast state, which further inhibits TCP phase formation.[16] Although Re increases dendrite segregation,[16] it enhances long-term stability by segregating to and thereby stabilizing the γ/γ' interfaces, hence reducing coarsening of γ' during creep.[52,53] However, this effect may be the result of a combination of Re with other alloying elements.[49] The comparatively low diffusivity of Re and W impedes precipitate coarsening.[2,5] Alloying for mechanical strength is generally detrimental to oxidation and corrosion resistance.[2,32] Compositions must hence be carefully tuned.

Spotlight: Role of W and Mo

Mo and W are primarily added for their effectiveness in increasing creep resistance.[51,54] While Mo preferentially partitions to the γ phase,[49,55] W is usually observed in both phases[18] with only a slight preference to γ. In fact, Amouyal et al.[56] showed that W preferentially occupies γ' Al sites but must compete for these with Ta. Since it is energetically favorable to push W into γ rather than Ta, above a certain (W+Ta) content the partitioning of W shifts to favor γ.

Mo increases the lattice parameter of γ without affecting γ', most strongly observed for low Re compositions.[55] The change in γ/γ' lattice misfit reduces dislocation spacing at the γ/γ' interface,[57–59] strengthening the alloy, retarding γ' coarsening,[60] lowering minimum creep rate and extending creep life.[54] This effect is pronounced when the γ phase is saturated in Mo whereas over-saturation can deteriorate the mechanical properties by precipitation of detrimental phases.[50,54]

Mo and W are not as effective in strengthening γ as Re. According to Fleischmann et al.,[61] 1 wt% Re would have to be substituted with 2.2 wt% Mo or 4.3 wt% W to keep a constant creep rate. Yet, Mo and W offer other advantages. Substitution of W and Re by Mo decreases the alloy density (i.e., the turbine weight)[7] and facilitates superalloy fabrication. While Re increases dendritic segregation, Mo reduces the segregation of W and hence shortens the homogenization heat treatment.[62] W has been shown to stabilize the γ/γ' interface and impede interface crack propagation at lower temperatures whereas at higher temperatures, W enhances the alloy ductility.[63] W also reduces precipitate coarsening due to its low diffusivity.[5]

Although Mo and W are added for their positive effect on creep resistance, excessive additions can promote TCP phase formation at elevated temperatures, degrading the alloy's high-temperature strength.[49,50,55] Even more prominent is their deleterious effect on oxidation and corrosion resistance. In some studies, Mo and W were shown to increase oxidation rate, leading to a less protective scale,[47,64] whereas in others, Mo was reported to decrease the oxidation rate.[64,65] In 1976, Peters et al.[66] observed substantially accelerated degradation at 900°C and the formation of a Mo-rich oxide for both salted and unsalted samples of ternary Ni–Cr–Mo alloys with high Mo contents. Their unsalted samples only exhibited rapid degradation in a static oxygen environment, whereas a flowing oxygen environment led to protective oxide scale formation. This observation was associated with the formation of volatile MoO_3, which can escape only from an unsalted sample in a flowing environment. Interestingly, similar corrosion was observed for both salted Ni–Cr alloys in a gaseous MoO_3 environment and for alloys coated with a mixture of Na_2MoO_4 and Na_2SO_4. The first observation suggests acidic fluxing through the reaction of $MoO_3 + Na_2SO_4 \rightarrow Na_2MoO_4 + SO_3$ (i.e., the formation of an acidic salt), whereas the salt in the latter observation is not expected to be acidic, suggesting that another mechanism may be responsible for the corrosion.[66] Multicomponent Ni-based superalloys exhibit accelerated oxidation and the formation of Mo oxide as well. In recent years, both Homaeian et al.[67] and Lutz et al.[47] found Na_2MoO_4 in the corrosion product, which they linked to the previously mentioned reaction of MoO_3 with Na_2SO_4 and consequently to acidic fluxing. Lutz et al. showed that while corrosion only occurred for salted samples, no gaseous SO_3 environment was needed even at a temperature as low as 700°C, which further supports an alloy-induced acidic fluxing mechanism.[47] Additionally, the volatility of MoO_3 can lead to voids and cracks in the oxide scale as MoO_3 evaporates.[67]

Contributions of atom probe tomography and correlative microscopy

Superalloys entail a high degree of alloying, with elemental compositions ranging from trace amounts to several wt%, and the precipitation of micro- and nanoscale phases with elemental segregation to interfaces and grain boundaries. To understand these complex alloys, a range of investigation tools are needed for characterization from millimeter- to nanometer-length scales. SEM imaging can effectively be used for large-scale analysis such as identifying grain size, precipitate microstructures and the presence of additional phases such as TCP phases, and is complemented by techniques such as EDX, x-ray photoelectron spectroscopy (XPS), and nanoscale secondary ion mass spectrometry (NanoSIMS) for characterization of chemical composition. For more detailed characterization of smaller features on

nanometer length scales however, high-resolution investigation tools such as TEM and atom probe tomography (APT) are needed.[68,69] APT provides unparalleled knowledge of the alloying elements' precise location within the alloy, promoting fundamental understanding of the interplay between alloying additions and their role in superalloy properties. APT is best suited for in-depth studies of 3D near-atomic-scale elemental distributions, thanks to its high spatial resolution and elemental sensitivity.[15,70]

In recent years, APT has been employed in high-resolution investigations of nanoscale features of Ni-superalloys. This includes studies of the chemical composition of phases, tracing compositional changes across phase interfaces,[15,68] and determining the elemental partitioning between phases, giving unprecedented insight in phase formation and interface strengthening mechanisms.[15,18] Lapington et al.[68] observed W segregation at γ-γ′ interfaces for the first time, likely due to the element's slow diffusion and hence accumulation during precipitate formation and growth. In polycrystalline alloys, GB segregation studies performed with APT revealed the segregation of B as well as Mo, leading to boride formation above a threshold of segregation.[15,69,71] The study by Kontis et al.[71] showed that boron additions of 0.05 wt% extended the sample lifetime from 90 to 9000 h in creep tests. To characterize the effect of boron in Ni-superalloys, correlative microscopy using SEM, TEM, APT, and NanoSIMS was applied. Combined SEM and TEM analysis identified inter- and intragranular carbides in low B-containing alloys, and borides in alloys with higher B-content. All phase compositions were studied with APT, revealing Cr-enrichment within the carbides/borides. Complementary NanoSIMS, which is sensitive to low concentration elements such as B over larger volumes than APT, enabled the characterization of boride size and distribution along grain boundaries, confirming predominant partitioning of B into borides without any indication of GB segregation or dissolution into the matrix.

Precipitates can form in various sizes at different stages of alloy fabrication. APT has been used to identify and investigate precipitates such as γ′ phase particles found within the γ phase channels.[15,68,69] Tertiary precipitates of the polycrystalline alloy RR1000 exhibit a notably different phase chemistry than both the primary and secondary precipitates, despite having the same nominal chemical composition, with higher compositional values of Mo and Al at reduced Ti, Ta, and Hf compositions. Obviously, the γ′ precipitate size, distribution, and composition depends strongly on the different heat-treatment stages during fabrication (i.e., the different temperatures and times).[69] The high resolution of APT has allowed to precisely identify the onset of precipitation during thermal aging as well as to monitor the evolution of precipitate composition and morphology.[72]

Another powerful aspect of APT is the ability to investigate lattice site elemental occupancies in 3D.[69] If the crystallographic planes are visible in the reconstruction (e.g., if the <100> crystal direction roughly aligns with the analysis direction), Ni-X Spatial Distribution Maps can be created, which show the distance between Ni atoms and other alloying elements. This analysis reveals which alloying elements occupy the Ni sublattice sites and which ones occupy the Al sublattice sites in the γ′ phase. While the latter is commonly occupied by Ti and Ta, Bagot et al.[69] also found Mo to preferentially occupy Al lattice sites, although this depends on the overall alloy composition. Lattice site segregation gives extremely important information that can be used to predict antiphase boundary energy and therefore overall alloy strength.

APT is often used alongside other microscopy techniques to investigate oxide formation in superalloys, both at surfaces and at crack tips, and to determine the location of contaminants such as sulfur and chlorine, therefore improving the fundamental understanding of the thermodynamic and kinetic driving forces behind environmental degradation.

Correlative microscopy studies of surface oxide formation identify distinct nanoscale oxides and their compositions. For example, using APT, focused ion beam (FIB), and XPS, it was shown that the addition of Mn to a superalloy produces an oxide scale comprised of several types of nanometer-scale oxides ($NiCr_2Mn_2O_4$, Cr_2O_3, $MnCr_2O_4$, $(Ti,Cr)O_2$) coexisting in an inhomogeneous mixture, which were previously, with other lower resolution techniques, identified as a homogeneous scale of intermediate composition.[11]

In a silicon-containing alloy, SEM and scanning transmission electron microscopy (STEM)-EDX showed the formation of a more continuous dual layer Al_2O_3, Cr_2O_3 surface scale, with nanoparticle silica formation at the interface detected with APT. This had not been observed with any other technique previously and opens new avenues of understanding of the role of silicon on oxidation kinetics of nickel-based superalloys.[38]

In a Ti-containing superalloy, SEM and APT revealed Ti enrichment and O depletion at chromia grain boundaries within the surface oxide scale, which gave insight into the oxide scale growth mechanisms: through outward diffusion of titanium, rather than inward diffusion of oxygen. This information was then used to calculate, based on the GB diffusion speed of titanium in chromia, how much the oxide scale would thicken every 24 h,[41] shown in **Figure 4**.

A B-containing superalloy was also studied using APT, and the results showed a surface aluminoborate phase within the oxide scale, which weakened the polycrystalline superalloy due to the outward diffusion of B from grain boundaries into the oxide scale.[39]

In another study, MC carbides were shown to initiate cracks as the oxidation products cause surface eruptions.[73]
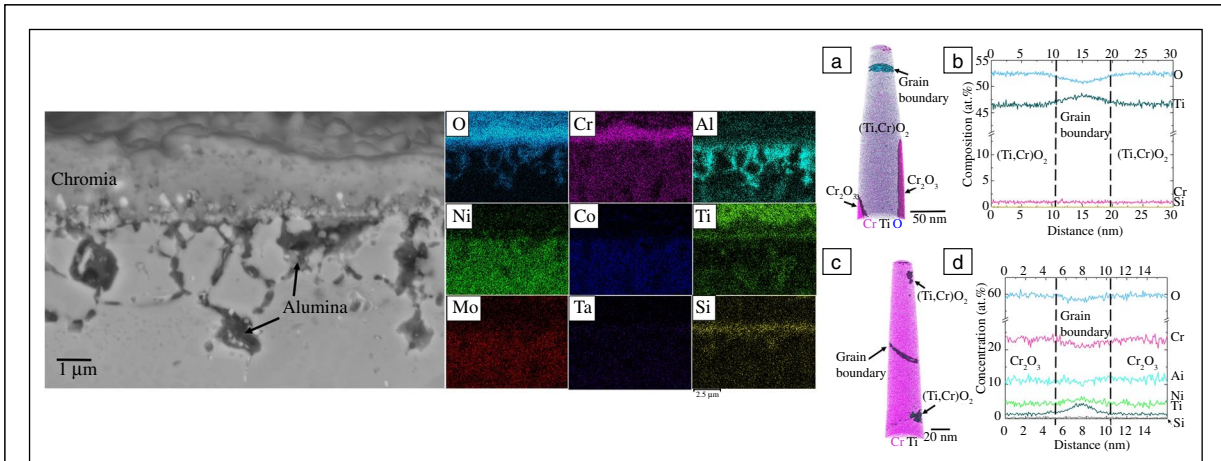
Figure 4. SEM micrograph of oxide scale on superalloy surface (left); EDX maps of same region indicating a Ti-rich outermost layer (center); APT reconstructions with 1D composition profiles through GBs (right): (a) AP needle taken from outer Ti-enriched rutile phase, (c) AP needle taken from chromia scale (b), (d) composition profiles through GB in (a, c), respectively, showing Ti enrichment at GBs; adapted and reprinted from Reference 41 with permission from Creative Commons Attribution 4.0 International License (http://creativecommons.org/licenses/by/4.0/).
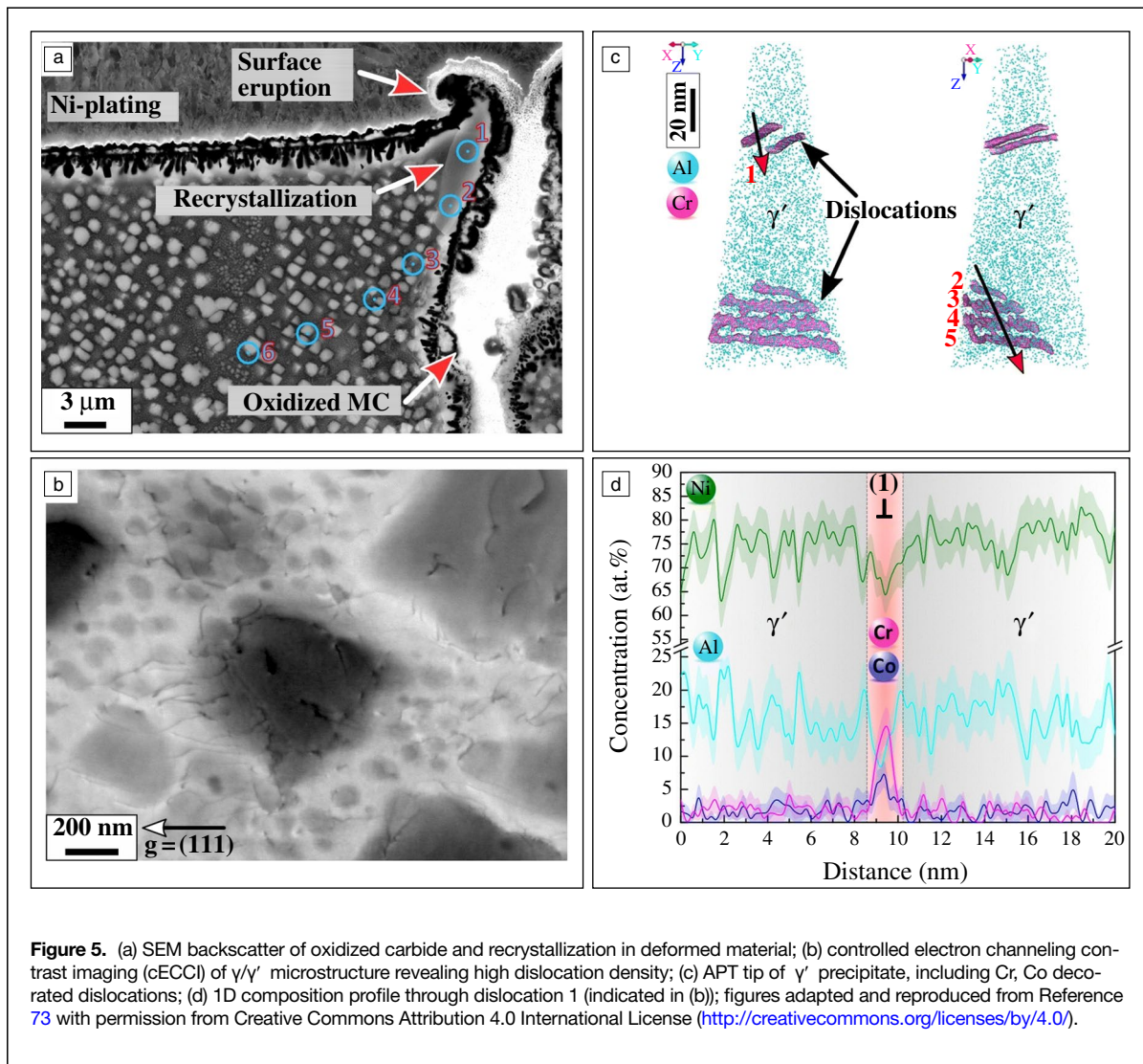
Figure 5. (a) SEM backscatter of oxidized carbide and recrystallization in deformed material; (b) controlled electron channeling contrast imaging (cECCI) of γ/γ′ microstructure revealing high dislocation density; (c) APT tip of γ′ precipitate, including Cr, Co decorated dislocations; (d) 1D composition profile through dislocation 1 (indicated in (b)); figures adapted and reproduced from Reference 73 with permission from Creative Commons Attribution 4.0 International License (http://creativecommons.org/licenses/by/4.0/).
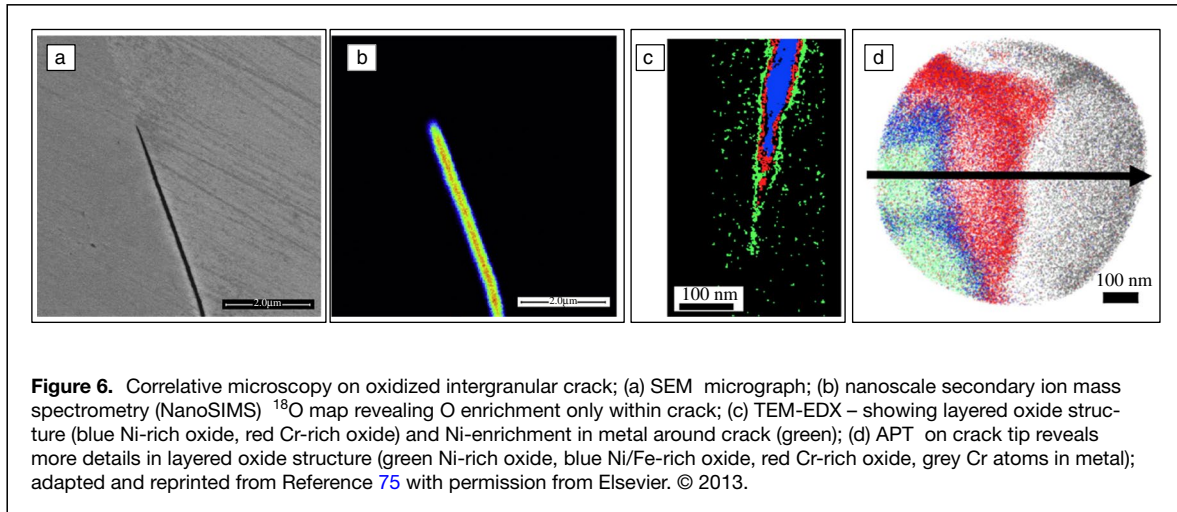
Figure 6. Correlative microscopy on oxidized intergranular crack; (a) SEM micrograph; (b) nanoscale secondary ion mass spectrometry (NanoSIMS) ^{18}O map revealing O enrichment only within crack; (c) TEM-EDX – showing layered oxide structure (blue Ni-rich oxide, red Cr-rich oxide) and Ni-enrichment in metal around crack (green); (d) APT on crack tip reveals more details in layered oxide structure (green Ni-rich oxide, blue Ni/Fe-rich oxide, red Cr-rich oxide, grey Cr atoms in metal); adapted and reprinted from Reference 75 with permission from Elsevier. © 2013.

Correlative SEM, controlled electron channeling contrast imaging (cECCI), and APT (**Figure 5**) has revealed a high density of Cr, Co decorated dislocations, enabling rapid Cr, Co transport through pipe diffusion, and γ′ precipitate dissolution due to local chemical inhomogeneities.

The investigation of crack tips using correlative microscopy with APT enabled the identification of alumina and chromia oxide intrusions ahead of crack tips[74] as well as the identification of layered oxide scales within the cracks,[12,75] offering new insights into the failure mechanisms. Using SEM and NanoSIMS (**Figure 6**a–b), Viskari et al.[75] found that oxygen enters intergranular cracks without penetrating into the GB ahead of the crack tip, nor into the adjacent grains, as was verified by APT. The layered oxide within the crack comprises mainly a Ni-rich oxide layer and a Cr-rich oxide layer as identified by XPS and TEM–EDX on a broad scale, and higher precision APT on the crack tip itself (Figure 6c, d). All characterization techniques were in agreement with each other, however, APT exhibited markedly the greatest detail, revealing three distinct regions within the Ni-rich oxide (Co-enrichment in outermost layer, Fe-enrichment in innermost layer) and thin, incontinuous Al- and Nb-rich oxides between the Cr-rich oxide layer and the metal.[75]
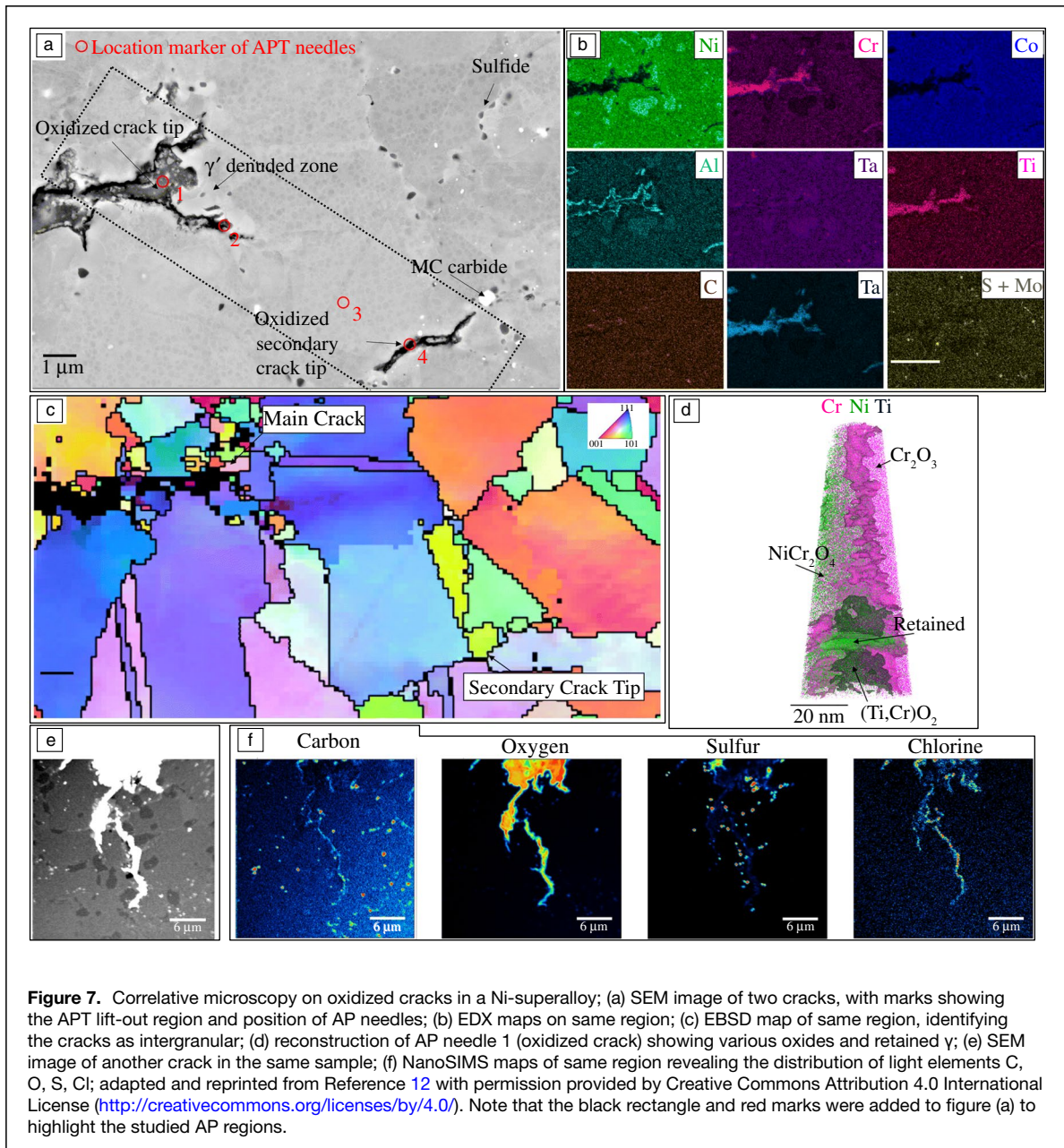
Pedrazzini et al.[12] investigated the effect of gaseous SO$_x$ and salt on corrosion-assisted cracks using SEM for identification of cracks and oxidized regions in the material, electron backscatter diffraction (EBSD) to confirm the intergranular nature of the cracks, EDX for large-scale compositional analysis, complemented by NanoSIMS for improved detection of light elements (S, O, C, Cl), APT for precise compositional analysis of nanoscale segregation within the oxide, and TEM in combination with STEM-EDX to identify Cr-Ti sulfide particles at grain boundaries near the oxidized crack

(**Figure 7**). Their work showed that both the addition of SO$_x$ as well as salt accelerates corrosion and crack growth. However, the oxide scale within the cracks seem to inhibit sulfur contamination within the alloy. APT was used to prove that cracking and crack growth may be instigated by sulfur in the early stages, but it is later advanced mainly by the presence of oxygen.[12]

Conclusions

The ever-evolving environment of turbine engines leads to the need for future alloy development targeted for the specific applications. The current challenge in the development of new Ni-based superalloys for aero-engine applications is to design high-temperature creep-resistant alloys without compromising their corrosion resistance. Recent advances in instrumentation, including APT, have led to step-changes in understanding of the fundamental corrosion mechanisms that govern the failure of superalloys, although more work is needed. In particular, the mechanisms underlying the most recently observed corrosion below 600°C must be elucidated, as the role of individual alloying elements in this phenomenon is still not understood.

APT is an effective tool to investigate these complex Ni-based superalloys thanks to its high spatial and chemical resolution, in 3D, to the near-atomic scale. Determining where elements reside within the alloy, its oxide scale, or within cracks enables us to understand how these elements affect the superalloy properties and how they drive corrosion mechanisms. Correlating APT results with other microscopy techniques such as SEM, TEM, EDX, and NanoSIMS will substantially aid in the development of new, corrosion-resistant superalloys for increased efficiency aero-engines.

Figure 7. Correlative microscopy on oxidized cracks in a Ni-superalloy; (a) SEM image of two cracks, with marks showing the APT lift-out region and position of AP needles; (b) EDX maps on same region; (c) EBSD map of same region, identifying the cracks as intergranular; (d) reconstruction of AP needle 1 (oxidized crack) showing various oxides and retained γ; (e) SEM image of another crack in the same sample; (f) NanoSIMS maps of same region revealing the distribution of light elements C, O, S, Cl; adapted and reprinted from Reference 12 with permission provided by Creative Commons Attribution 4.0 International License (http://creativecommons.org/licenses/by/4.0/). Note that the black rectangle and red marks were added to figure (a) to highlight the studied AP regions.

Author contributions
C.R. completed the literature review and wrote the paper; M.A., M.P.R., and S.P. supervised and contributed to the paper writing.

Data availability
Sources used in this review are available in the literature and appropriately referenced, and each source will have its own data policy.

Code availability
Not applicable.

Conflict of interest
The authors have no conflict of interest to declare.

Open Access

References

1. R.C. Reed, *The Superalloys: Fundamentals and Applications* (Cambridge University Press, New York, 2006)
2. R. Darolia, *Int. Mater. Rev.* (2019). https://doi.org/10.1080/09506608.2018.1516713
3. R. M'Saoubi, D. Axinte, S.L. Soo, C. Nobel, H. Attia, G. Kappmeyer, S. Engin, W.-M. Sim, *CIRP Ann.–Manuf. Technol.* **64**(2), 557 (2015). https://doi.org/10.1016/j.cirp.2015.05.002
4. K. Kawagishi, A.C. Yeh, T. Yokokawa, T. Kobayashi, Y. Koizumi, H. Harada, *Superalloys 2012* (2012). https://doi.org/10.1002/9781118516430.ch21
5. H. Long, S. Mao, Y. Liu, Z. Zhang, X. Han, *J. Alloy Compd.* (2018). https://doi.org/10.1016/j.jallcom.2018.01.224
6. P. Caron, *Superalloys 2000* (2000). https://doi.org/10.7449/2000/Superalloys_2000_737_746
7. R.A. MacKay, T.P. Gabb, J.L. Smialek, M.V. Nathal, *JOM* (2010). https://doi.org/10.1007/s11837-010-0011-0
8. N. Eliaz, G. Shemesh, R.M. Latanision, *Eng. Fail. Anal.* (2002). https://doi.org/10.1016/S1350-6307(00)00035-2
9. L. Brooking, S. Gray, K. Dawson, J.R. Nicholls, N.J. Simms, J. Sumner, G.J. Tatlock, *Corros. Sci.* (2020). https://doi.org/10.1016/j.corsci.2019.108293
10. B. Gault, M.P. Moody, J.M. Cairney, S.P. Ringer, *Atom Probe Microscopy,* Springer Series in Materials Science, vol. 160 (Springer, New York, 2012). https://doi.org/10.1007/978-1-4614-3436-8
11. S. Pedrazzini, D.J. Child, G. West, S.S. Doak, M.C. Hardy, M.P. Moody, P.A.J. Bagot, *Scr. Mater.* **113**, 51 (2016). https://doi.org/10.1016/j.scriptamat.2015.10.001
12. S. Pedrazzini, D.J. Child, T. Aarholt, C. Ball, M. Dowd, A. Girling, H. Cockings, K. Perkins, M.C. Hardy, H.J. Stone, P.A.J. Bagot, *Metall. Mater. Trans. A* **49**, 3908 (2018). https://doi.org/10.1007/s11661-018-4752-7
13. M. Meisnar, M. Moody, S. Lozano-Perez, *Corros. Sci.* **98**, 661 (2015). https://doi.org/10.1016/j.corsci.2015.06.008
14. T.M. Pollock, S. Tin, *J. Propuls. Power.* (2006). https://doi.org/10.2514/1.18239
15. M.K. Miller, *Micron* (2001). https://doi.org/10.1016/S0968-4328(00)00083-4
16. R.M. Kearsey, J.C. Beddoes, P. Jones, P. Au, *Intermetallics* **12**, 903 (2004). https://doi.org/10.1016/j.intermet.2004.02.041
17. Z.X. Shi, J.R. Li, S.Z. Liu, X.G. Wang, *Trans. Nonferrous Met. Soc. China* (2014). https://doi.org/10.1016/S1003-6326(14)63380-X
18. R.C. Reed, A.C. Yeh, S. Tin, S.S. Babu, M.K. Miller, *Scr. Mater.* (2004). https://doi.org/10.1016/j.scriptamat.2004.04.019
19. H. Long, Y. Liu, S. Mao, H. Wei, J. Zhang, S. Ma, Q. Deng, Y. Chen, Z. Zhang, X. Han, *Scr. Mater.* (2018). https://doi.org/10.1016/j.scriptamat.2018.07.041
20. C.Z. Hargather, S.-L. Shang, Z.-K. Liu, *Data Brief* **20**, 1537 (2018). https://doi.org/10.1016/j.dib.2018.08.144
21. A.S. Wilson, *Mater. Sci. Technol.* (2016). https://doi.org/10.1080/02670836.2016.1187335
22. C.M.F. Rae, M.S.A. Karunaratne, C.J. Small, R.W. Broomfield, C.N. Jones, R.C. Reed, *Superalloys 2000* (2000). https://doi.org/10.7449/2000/SUPERALLOYS_2000_767_776
23. A. Volek, R.F. Singer, *Superalloys 2004* (2004). https://doi.org/10.7449/2004/Superalloys_2004_713_718
24. M.S.A. Karunaratne, C.M.F. Rae, R.C. Reed, *Metall. Mater. Trans. A* (2001). https://doi.org/10.1007/s11661-001-0032-y
25. J. Chen, J. Chen, Q. Wang, Y. Wu, Q. Li. C. Xiao, X. Hui, *Mater. Lett.* **312**, 131656 (2022). https://doi.org/10.1016/j.matlet.2022.131656
26. M. Pessah, P. Caron, T. Khan, *Superalloys 1992* (1992). https://doi.org/10.7449/1992/superalloys_1992_567_576
27. M. Simonetti, P. Caron, *Mater. Sci. Eng. A* (1998). https://doi.org/10.1016/S0921-5093(98)00766-7
28. Z. Zhang, Z. Yue, *J. Alloys Compd.* (2018). https://doi.org/10.1016/j.jallcom.2018.02.133
29. Y. Zheng, S. Li, L. Zheng, Y. Han, *Superalloys 2004* (2004). https://doi.org/10.7449/2004/Superalloys_2004_743_751
30. T. Zhou, W. Feng, H. Zhao, Y. Meng, H. Zhang, H. Ding, Z. Wang, *Prog. Nat. Sci. Mater. Int.* (2018). https://doi.org/10.1016/j.pnsc.2017.12.003
31. M.P. Brady, I.G. Wright, B. Gleeson, *JOM* (2000). https://doi.org/10.1007/s11837-000-0109-x
32. B. Gleeson, in *Materials Science and Technology: A Comprehensive Treatment*, R.W. Cahn, P. Haasen, E.J. Kramer, Eds. (Wiley, Weinheim, 2000), p. 173
33. D.J. Young, *High Temperature Oxidation and Corrosion of Metals*, 1st ed. (Elsevier, Amsterdam, 2008)
34. X. Liu, B. Gleeson, *Mater. High Temp.* (2015). https://doi.org/10.1179/0960340914Z.00000000055
35. B.S. Mitchell, *An Introduction to Materials Engineering and Science for Chemical and Materials Engineers* (Wiley, New York, 2004) pp. 179–182
36. M. Bensch, A. Sato, N. Warnken, E. Affeldt, R.C. Reed, U. Glatzel, *Acta Mater.* (2012). https://doi.org/10.1016/j.actamat.2012.06.036
37. R.V. Miner Jr., C.E. Lowell, *Effects of Silicon Additions on Oxidation and Mechanical Behavior of the Nickel-Base Superalloy B-1900* (NASA Technical Note TN-D7989, 1975)
38. A. Sato, Y. Chiu, E.A. Marquis, R.C. Reed, *Mater. High Temp.* **29**(3), 272 (2012). https://doi.org/10.3184/096034012X13335334078005
39. P. Kontis, S. Pedrazzini, Y. Gong, P.A.J. Bagot, M.P. Moody, R.C. Reed, *Scr. Mater.* **127**, 156 (2017). https://doi.org/10.1016/j.scriptamat.2016.09.013
40. S. Cruchley, H.E. Evans, M.P. Taylor, M.C. Hardy, S. Stekovic, *Corros. Sci.* **75**, 58 (2013). https://doi.org/10.1016/j.corsci.2013.05.016
41. S. Pedrazzini, B.S. Rowlands, A. Turk, I.M.D. Parr, M.C. Hardy, P.A.J. Bagot, M.P. Moody, E. Galindo-Nava, H.J. Stone, *Metall. Mater. Trans. A*, **50**, 3024 (2019). https://doi.org/10.1007/s11661-019-05246-5
42. X. Montero, A. Ishida, T.M. Meiÿner, H. Murakami, M.C. Galetz, *Corros Sci.* (2020). https://doi.org/10.1016/j.corsci.2020.108472
43. R.A. Rapp, *Corros. Sci.* (2002). https://doi.org/10.1016/S0010-938X(01)00057-9
44. E. Kistler, W.T. Chen, G.H. Meier, B. Gleeson, *Mater. Corros.* (2019). https://doi.org/10.1002/maco.201810751
45. K.L. Luthra, *Metall. Trans. A* (1982). https://doi.org/10.1007/BF02647842
46. L. Brooking, J. Sumner, S. Gray, N.J. Simms, *Mater. High Temp.* (2018). https://doi.org/10.1080/09603409.2017.1392414
47. B.S. Lutz, J.M. Alvarado-Orozco, L. Garcia-Fresnillo, G.H. Meier, *Oxid. Met.* (2017). https://doi.org/10.1007/s11085-017-9746-0
48. F. Duarte Martinez, N.I. Morar, M. Kothari, G. Gibson, J. Leggett, J.C. Mason-Flucke, J.R. Nicholls, G.M. Castelluccio, S. Gray, *Superalloys 2020* (2020). https://doi.org/10.1007/978-3-030-51834-9_73
49. W. Xia, X. Zhao, L. Yue, Z. Zhang, *J. Mater. Sci Technol.* (2020). https://doi.org/10.1016/j.jmst.2020.01.026
50. R.A. MacKay, M.V. Nathal, D.D. Pearson, *Metall. Trans. A* (1990). https://doi.org/10.1007/BF02782418
51. R. Sowa, S. Arabasz, M. Parlinska-Wojtan, *Zaštita Mater.* (2016). https://doi.org/10.5937/ZasMat1602274S
52. Q. Ding, S. Li, L.-Q. Chen, X. Han, Z. Zhang, Q. Yu, J. Li, *Acta Mater.* (2018). https://doi.org/10.1016/j.actamat.2018.05.025
53. W. Xia, X. Zhao, L. Yue, Z. Zhang, *J. Alloys Compd.* (2020). https://doi.org/10.1016/j.jallcom.2019.152954
54. J. Zhang, J. Li, T. Jin, X. Sun, Z. Hu, *Mater. Sci. Eng. A* (2010). https://doi.org/10.1016/j.msea.2010.01.045
55. R.A. MacKay, T.P. Gabb, A. Garg, R.B. Rogers, M.V. Nathal, *Mater. Charact.* (2012). https://doi.org/10.1016/j.matchar.2012.05.001
56. Y. Amouyal, Z. Mao, D.N. Seidman, *Acta Mater.* (2010). https://doi.org/10.1016/j.actamat.2010.07.004
57. J.X. Zhang, T. Murakumo, Y. Koizumi, T. Kobayashi, H. Harada, S. Masaki, *Metall. Mater. Trans. A* (2002). https://doi.org/10.1007/s11661-002-0246-7
58. Y. Koizumi, T. Kobayashi, T. Yokokawa, J. Zhang, M. Osawa, H. Harada, Y. Aoki, M. Arai, *Superalloys 2004* (2004). https://doi.org/10.7449/2004/Superalloys_2004_35_43
59. X.G. Liu, L. Wang, L.H. Lou, J. Zhang, *J. Mater. Sci. Technol.* (2015). https://doi.org/10.1016/j.jmst.2013.12.019
60. G.S. Shin, J.Y. Yun, M.C. Park, S.J. Kim, *Mater. Charact.* (2014). https://doi.org/10.1016/j.matchar.2014.06.019
61. E. Fleischmann, M.K. Miller, E. Affeldt, U. Glatzel, *Acta Mater.* (2015). https://doi.org/10.1016/j.actamat.2014.12.011

62. E.C. Caldwell, F.J. Fela, G.E. Fuchs, *JOM* (2004). https://doi.org/10.1007/s11837-004-0200-9
63. S.L. Liu, C.Y. Wang, T. Yu, *RSC Adv.* (2015). https://doi.org/10.1039/C5RA07323E
64. S.J. Park, S.M. Seo, Y.S. Yoo, H.W. Jeong, H. Jang, *Materials* (2019). https://doi.org/10.3390/ma12182934
65. S.T. Mileiko, N.I. Novokhatskaya, *J. Mater. Eng. Perform.* (2015). https://doi.org/10.1007/s11665-014-1305-0
66. K.R. Peters, D.P. Whittle, J. Stringer, *Corros. Sci.* (1976). https://doi.org/10.1016/0010-938X(76)90010-X
67. A. Homaeian, M. Alizadeh, *Eng. Fail. Anal.* (2016). https://doi.org/10.1016/j.engfailanal.2016.03.012
68. M.T. Lapington, D.J. Crudden, R.C. Reed, M.P. Moody, P.A.J. Bagot, *Metall. Mater. Trans. A*, **49**, 2302 (2018). https://doi.org/10.1007/s11661-018-4558-7
69. P.A.J. Bagot, O.B.W. Silk, J.O. Douglas, S. Pedrazzini, D.J. Crudden, T.L. Martin, M.C. Hardy, M.P. Moody, R.C. Reed, *Acta Mater.* **125**, 156 (2017). https://doi.org/10.1016/j.actamat.2016.11.053
70. D. Blavette, E. Cadel, B. Deconihout, *Mater. Charact.* **44**, 133 (2000). https://doi.org/10.1016/S1044-5803(99)00050-9
71. P. Kontis, H.A. Mohd Yusof, S. Pedrazzini, M. Danaie, K.L. Moore, P.A.J. Bagot, M.P. Moody, C.R.M. Grovenor, R.C. Reed, *Acta Mater.* **103**, 688 (2016). https://doi.org/10.1016/j.actamat.2015.10.006
72. H. Gardner, S. Pedrazzini, J.O. Douglas, D. De Lille, M.P. Moody, P.A.J. Bagot, *Metall. Mater. Trans. A* **50**, 1862 (2019). https://doi.org/10.1007/s11661-018-5098-x
73. P. Kontis, Z. Li, M. Segersäll, J.J. Moverare, R.C. Reed, D. Raabe, B. Gault, *Metall. Mater. Trans. A* **49**, 4236 (2018). https://doi.org/10.1007/s11661-018-4709-x
74. H.S. Kitaguchi, M.P. Moody, H.Y. Li, H.E. Evans, M.C. Hardy, S. Lozano-Perez, *Scr. Mater.* **97**, 41 (2015). https://doi.org/10.1016/j.scriptamat.2014.10.025
75. L. Viskari, M. Hörnqvist, K.L. Moore, Y. Cao, K. Stiller, *Acta Mater.* **61**(10), 3630 (2013). https://doi.org/10.1016/j.actamat.2013.02.050 ☐

M. Appleton is a materials technologist in the Surface Engineering Group at Rolls-Royce plc, where he works on environmental protection of gas-turbine engines. He graduated with an EngD degree (Hons) from the University of Cambridge, UK, in 2016. His current role involves aspects of failure investigation and service-run condition assessment of turbine hardware, R&D programs, as well as manufacturing support across a range of turbine technologies. Current work-streams involve mitigation of corrosion-fatigue and calcium magnesium alumino-silicates (CMAS)-attack using novel coating technology. Appleton can be reached by email at matt.appleton@rolls-royce.com.

M.P. Ryan CBE, FREng, is the Armourers & Brasiers' Chair in Materials Science and Nanotechnology at Imperial College London, UK, and Interim Vice-Provost for Research and Enterprise in the Faculty of Engineering. She joined Imperial College in 1998 from Brookhaven National Laboratory. She graduated from The University of Manchester with a joint Honours degree in mathematics and physics and was then awarded a PhD degree in materials science carrying out early work with *in situ* electrochemical scanning tunneling microscopy to study passivation phenomena in binary alloy systems. Ryan can be reached by email at m.p.ryan@imperial.ac.uk.

C. Rodenkirchen is a doctoral candidate in the Department of Materials at Imperial College London, UK. Her research focuses on the effect of alloying elements on the properties of Ni-based superalloys, with particular interest in hot-corrosion resistance. She received her MSc and BSc degrees in physics at the RWTH Aachen University, where she specialized in experimental condensed-matter physics and researched the role of nanostructuring on thermoelectric materials using atom probe tomography at the I. Institute of Physics. Rodenkirchen can be reached by email at c.rodenkirchen20@imperial.ac.uk.

S. Pedrazzini is a lecturer in engineering alloys and metallurgy, Engineering and Physical Sciences Research Council Early Career Fellow, and Royal Academy of Engineering Associate Research Fellow at Imperial College London, UK. She runs a research group on the environmental degradation of engineering alloys, with a particular interest in oxidation and hot corrosion of nickel- and cobalt-based superalloys, aqueous corrosion of steel as well as advanced characterization techniques such as transmission electron microscopy and atom probe tomography. Pedrazzini can be reached by email at s.pedrazzini@imperial.ac.uk.